Effect of AC field on uniaxial viscosity and sintering stress of ceria

Chen Cao[1] (ORCiD: https://orcid.org/0000-0001-9496-0528), c.cao@fz-juelich.de

Robert Mücke[1], r.muecke@fz-juelich.de

Olivier Guillon[1] (ORCiD: https://orcid.org/0000-0003-4831-5725), o.guillon@fz-juelich.de

[1]:Institut für Energie und Klimaforschung (Institute of Energy and Climate Research), IEK-1: Werkstoffsynthese und Herstellungsverfahren (Materials Synthesis and Processing), Forschungszentrum Jülich GmbH, D-52425 Jülich, Germany

Abstract

The production of traditional and advanced ceramics is an energy-intensive activity, which requires high temperatures and long dwelling times to activate diffusional processes necessary for densification. Electric field assisted processing has received considerable attention recently, due to its potential to significantly reduce the costs of required heat treatments. However, the effect of electric fields on the densification and coarsening of oxide ceramics still not completely understood, and the mechanisms behind, in particular for fields, are still under debate. The potential influence of electric field on the sintering parameters (uniaxial viscosity and uniaxial sintering stress) and microstructure of polycrystalline yttria doped ceria were studied. Sintering parameters were measured without and with AC electric fields (14 V/cm and 28 V/cm, 50 Hz) which were below the “flash regime”. During all sintering measurements, the sample temperature was adjusted by lowering the furnace temperature according to the temperature measurements using densified samples. Major findings are: (i) The densification behavior is clearly modified by these moderate electric fields, although temperature increase due to macroscopic Joule heating is excluded. (ii) The

densification rate remains proportional to the applied stress under electrical fields. (iii) Sintering parameters are significantly affected by the applied electric fields.

Keywords

Ceria, sinter-forging, electric field assisted sintering, uniaxial viscosity, sintering stress

1 Introduction

The sintering of ceramic powder compacts to form products with desired properties requires a significant amount of energy. In order to reduce this required energy as well as to target unique properties required for applications, different approaches have been applied, including the usage of electric fields [1-3]. One example is the usage of low voltage together with high current density which is referred to as the field assisted sintering/spark plasma sintering technique (FAST/SPS) [1-2]. For materials with significantly lower electrical conductivity than the graphite tool, the comparison with hot pressing under the same conditions showed that there is no direct effect of the electrical fields, as evidenced for alumina [4] and fully stabilized zirconia [5]. The improvement in the sintering behavior was attributed to the mechanical compressive load and the high heating rates involved. For other ceramic systems in which high-electric currents flow directly through the green body rather than through the surrounding (graphite) tools, the higher sinterability has been related to the interactions between current and microstructural properties, such as Joule heating [2,6], percolation effects [7-8] and electrochemical reactions[9-10]. The usage of higher electric fields than in FAST/SPS without additional mechanical load refers to flash sintering, during which the densification occurs within a few seconds [3,11]. Many hypotheses have been proposed to explain this phenomenon. One hypothesis is attributing the amplified mass transport to a facilitated defect generation under electric fields [3,11-12]. However, atomistic simulations have shown that the electric field strength required to generate anti-Frenkel pairs (oxygen vacancies and oxygen interstitials) is beyond practical relevance. The required electrical field strength for monoclinic and cubic HfO_2 was found to be about 0.1 GV/cm, that is to apply 10^7 V to a 1 mm thick sample [13]. This value is beyond the dielectric strength of the materials and far higher than the field strengths used so far in

flash sintering experiments. Under relatively low electric fields (typically around 100 V/cm), studies show already a field related improvement of sintering for many ceramics. Therefore, another approach, the thermal run-away model, was proposed, which has successfully predicted the critical threshold of the electrical field as a function of the furnace temperature to trigger flash sintering [14-17]. According to this model, the Joule heating effects, especially macroscopic bulk Joule heating, are considered to be the main reason for the onset of flash sintering. As the supporting evidence for the assumption, experimental results showed that a material can undergo an instantaneous densification process, similar to flash sintering, caused solely by a pure thermal run-away introduced by other methods without electrical fields, but with a rapid heating rate [18]. This high heating rate yields a significant improvement in sintering and emphasizes the role of rapid heating behavior during flash sintering [19].

However, Joule heating cannot explain every phenomenon taking place during field assisted sintering. For example, the change of the electrical response of grain boundaries was found under DC flash sintering [20], but not under AC flash sintering [21]. The type and concentration of defects in ZnO is irreversibly modified by electric fields, even if no current flows through the sample [22]. Vendrell et al. found out that the ionic conductivity of flash-sintered Yttria-stabilized zirconia (YSZ) increased with the increased current density limit which was set prior to flash and attributed this phenomenon to a change in YSZ defect structure [23]. Thus, not a single mechanism should be expected to describe all effects during field assisted sintering. A combination of different mechanisms seems to be a more reasonable approach, with one of them dominating for a given material at a certain condition. To investigate it in a systematic way, the main issue to be addressed is the measurement of the true sample temperature. The dramatic temperature change during flash sintering renders the measurement of the sample temperature rather difficult. The most frequently used methods are infrared cameras and pyrometers which only provide temperature values of the sample surface. The inner temperature of the sample can be much higher if massive and rapid Joule heating is present. This issue hinders a clear separation of thermal and athermal effects.

In this work, weak electric fields, significantly lower than those required for the 'flash regime', were applied on free standing doped ceria samples, i.e without a graphite die in an instrumented sinter-forging device. Instead of DC electrical field, AC electrical fields were applied, in order to avoid potential inhomogeneities and gradients in composition and microstructure. The constant highest temperature inside the densified sample was set up as a benchmark for the following measurements. This was accomplished by adjusting the furnace temperature, in order to eliminate the temperature increase owing to the flow of electrical current. The temperature within the densified sample was also simulated using the thermo-electric finite element method for a complete understanding of the temperature distribution inside the sample. Once the temperature is controlled, densification rates, diffusion coefficients as well as sintering parameters can be reliably determined by instrumental sinter-forging [23-25]. The dependence of sintering parameters on the applied electrical fields, excluding the macroscopic Joule heating induced temperature increase, was investigated in this work for the first time, enabling an accurate identification of possible mechanisms during the field assisted sintering.

2 Theoretical Background

The similarity between sintering and creep processes allows the use of continuum mechanics to describe the response of sintering compacts under different constraints, for example, externally applied stress [25-29]. First, it is assumed that the material has a linear viscous behavior under external stresses. Secondly, the material is assumed to be isotropic and the sintering mechanism is not to be changed by the applied stress. This fits well with the low pressure experiments conducted in this work, where the applied stress is in the range of the sintering stress [23]. The constitutive equations for an isotropic, linear viscous material in the cylindrical coordinates can be thus written as follows:

$$\dot{\epsilon_r} = \dot{\epsilon_f} + \left(\frac{1}{E_p}\right)\left[\sigma_r - \upsilon_p(\sigma_\theta + \sigma_z)\right] \tag{2-1}$$

$$\dot{\epsilon_z} = \dot{\epsilon_f} + \left(\frac{1}{E_p}\right)\left[\sigma_z - \upsilon_p(\sigma_\theta + \sigma_r)\right] \tag{2-2}$$

where σ_r, σ_z and σ_θ are the stress components along the principal axes, $\dot{\epsilon_f}$: the free strain rate without any constraints, υ_p the viscous Poisson's ratio and E_p is the uniaxial viscosity. In the case of uniaxial stress applied along the z axis of a cylindrical sample, Eq. 2-1 and 2-2 reduce to:

$$\dot{\epsilon_r} = \dot{\epsilon_f} - \left(\frac{\upsilon_p}{E_p}\right)\sigma_z \tag{2-3}$$

$$\dot{\epsilon_z} = \dot{\epsilon_f} + \left(\frac{1}{E_p}\right)\sigma_z \tag{2-4}$$

The uniaxial viscosity is expressed as the following relationship derived from Eq. 2.4:

$$E_p = \frac{\sigma_z}{\dot{\epsilon_z} - \dot{\epsilon_f}} \tag{2-5}$$

The uniaxial viscosity can be experimentally determined from the slope of uniaxial strain rate – stress curve. The uniaxial viscosity increases with increasing relative density. The increase of uniaxial viscosity is a result of both grain growth and increasing relative density. In the case of polycrystalline materials, the uniaxial viscosity at a constant temperature can be expressed in the following general form [30]:

$$E_p = E_{p0} \times E_{p1}(\rho) \times E_{p2}(d) \times E_{p3}(T) \tag{2-6}$$

where E_{p0} is a scaling factor, E_{p1}, E_{p2} and E_{p3} are functions of relative density ρ, grain size d and temperature T, respectively.

The sintering stress or sintering potential Σ, as driving force for the densification, is related to the grain size, pore size, surface energy and grain boundary energy [31]. The relationship between sintering potential Σ and uniaxial sintering stress can be expressed as [23]:

$$\Sigma = \frac{\sigma_z^S}{1-2\upsilon_p} \tag{2-7}$$

The uniaxial sintering stress is a mathematical concept, which is the equivalent externally applied compressive stress that causes the same effect during free sintering as the surface energy of pores and grain boundaries [29,32]. The uniaxial sintering stress σ_z^s is experimentally determined by the extrapolation of the linear relation between uniaxial strain rate vs. uniaxial stress until the uniaxial strain rate equals to zero [26], which can be described as follows

$$\sigma_z^s = -\dot{\epsilon_f} E_p \quad (2\text{-}8)$$

The magnitude of uniaxial sintering stress varies among material systems from around 0.1 MPa for Low Temperature Co-fired Ceramics (LTCC) [24] and calcium aluminosilicate (CAS) glass [33], to a few MPa for submicron alumina [23], until up to 100 MPa in nanocrystalline zirconia [34-35]. The absolute value of the sintering stress increases during the intermediate stage of sintering and then starts to decrease on the transition from intermediate sintering to the final stage of sintering. However, agglomerates and inhomogeneities in powder compacts shift the beginning of the grain growth to relative densities lower than 90 % and thus can affect the viscosity/sintering stress-density relationship [34].

3 Experimental and Simulation Methods

3.1 Experimental Procedure

In this work, custom made loading dilatometry equipment was used as already published other studies [23-25]. This device was equipped with an independent programmable power source (ACS-2200-PS from HBS Electronic GmbH, Brühl, Germany). The controllable mechanical load (10 N - 160 N) was applied with an electromechanical testing system (model 5565, Instron, Norwood, USA) with an accuracy of 0.1 N. The radial and axial strains during sintering were optically measured by two laser scanners (Model 162-100, Beta LaserMike, Dayton, USA), allowing a dynamic resolution of about 2 µm. The instantaneous relative density, $\bar{\rho}$, during the experiments was calculated automatically on the basis of the measured data:

$$\bar{\rho} = \frac{\rho_0}{\rho_{th}.\exp(2\varepsilon_r+\varepsilon_z)} \quad \textbf{(3-1)}$$

where ρ_{th} is the theoretical density and ρ_o is the green density.

3.1.1 Material and sample preparation

A commercially available 10 mol.% Yttria doped ceria (10YDC) nanocrystalline powder (CerPoTech, Norway) with a primary average crystallite size of 12 nm (based on XRD results) was used. To allow for particle coarsening and a more homogeneous particle size distribution, the as-delivered powder was calcined at 1150 °C for 3 h and milled in

ethanol for 72 h with a speed of 90 rpm using a tumble mixer. After calcination and grinding, the suspension was put to stand for 3h and dried. The obtained powder turned had an average particle size of 154 nm (base on laser diffraction results). Cylindrical specimens were first uniaxially pressed at 100 MPa and subsequently cold isostatically pressed at 300 MPa. The obtained cylinders of 10YDC were 14.804 mm ± 0.9 % in height and 9.39 mm ± 0.6 % in diameter, yielding a relative green density of 62 % ± 2 %. The samples were heated with a heating rate of 30 K/min and held at isothermal furnace temperature from 1188 °C to 1208 °C. As soon as the isothermal furnace temperature was reached, the subsequent measurements of the sintering parameters started.

3.1.2 Calibration of isothermal sample temperature

The temperature of a densified sample was 1208 ± 2 °C for all sintering parameter measurements. To determine the different furnace temperatures yielding the same highest sample temperature under different electrical fields, a fully densified specimen (8.08 mm in diameter) with a 3 mm ± 0.05 mm depth hole drilled mechanically was used. Three thermocouples were installed (Figure 1): the thermocouple 1 was used to measure the furnace temperature (T1). An insulating mantle thermocouple was used to measure the temperature inside the sample (T2) and the third one was used to measure the temperature near the sample surface (T3), 2mm away from the sample surface. The thermocouples used in this study were all of type S with an accuracy of ± 1.5°C. The sample was heated to different furnace temperatures: 1100 °C, 1200 °C, 1300 °C, with 0 V/cm and field strength of E_{rms} = 14 V/cm, 21 V/cm, 28 V/cm and 42 V/cm until the temperature was stable. Each measurement was repeated two times. After the calibration, the isothermal temperature (T1) was set according to the specimen temperature (T2).

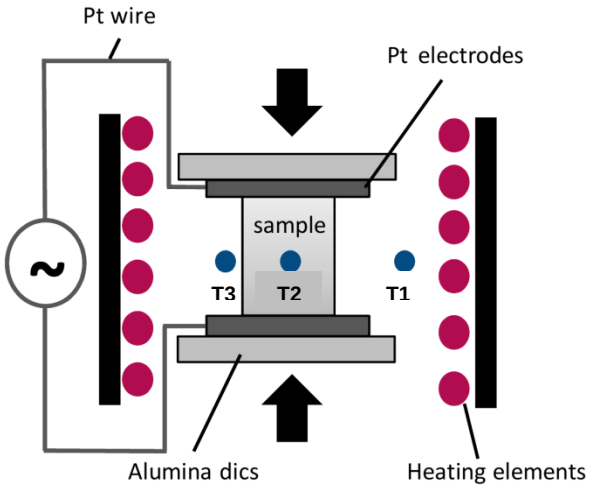

Figure 1: Schematic of the placement of thermocouples: T1: furnace; T2: inside sample; T3: near sample surface.

3.1.3 Sintering parameter measurement

All the free sintering experiments of this work were conducted under a minimal load of 10 N to maintain the contact between the electrodes and the specimen. Three different sets of experiments were designed to investigate the influence of electric field on sintering behavior. All these measurements were conducted under three different conditions of applied electrical fields E_{rms} = 0 V/cm, 14 V/cm and 28 V/cm with a frequency of 50 Hz.

(1) Discontinuous sinter-forging cycles were performed on samples freely sintered to a desired density of 70 %, 75 %, 80 % and 85 % during the isothermal period (1208 °C and 1188 °C) and then subjected to a constant load resulting in a pressure of 1.2 MPa and 2.4 MPa according to the specimen dimension at the beginning of the experiment. Considering the short duration of the load application, the pressure did not change much during the measurement. For example, for the discontinuous sinter-forging test under E_{rms} = 28 V/cm with 2.4 MPa at a relative density of 73 % (showing the highest sintering rate among all experiments), the pressure increased from 2.4 MPa to 2.49 MPa (4 %) due to radial shrinkage of the specimen. Similar consideration has been given to the electric field. Actually the voltage applied remains constant, but as the sample shrinks, the electric field increases, as shown in Figure 10. This mechanical loading was applied within a 3 % increase of relative density. These two pressure

values were chosen so that the anisotropy introduced by uniaxial mechanical load can be minimized. More than 20 sinter forging experiments were done, including two complete free sintering experiments at the same temperature. The true longitudinal axial strain was used considering the large deformation during the sintering. The sintering strain rates ($\dot{\varepsilon}_z$) of interest were then calculated using the derivation of an exponential fitting to curves of strain vs. time. The quality of the fitting was considered adequate when the coefficient of determination, R^2, was larger than 0.999.

(2) Specimens were sintered up to a relative density of 80 % and then cooled down for later microstructure analysis.

(3) To check the linearity relationship between axial strain rate and uniaxial stress, a third load of 4.8 MPa was applied under E_{rms} = 28 V/cm at the relative density of 80 %.

3.1.4 Microstructural characterization

After the above mentioned measurements, the final relative density was validated through Archimedes' method. Some samples were ground and polished to a 50 nm finish subsequently, the samples were thermally etched at a temperature 50 K lower than the sintering temperature for 1 hour. Finally, the samples were investigated using a scanning electron microscope, Zeiss Ultra55, (Carl Zeiss Microscopy, Oberkochen, Germany). Further, SEM images were imported into an image processing software (analySIS pro, Hamburg, Germany), applying a grain segmentation method for grain size analysis with a factor of 1.6 [36]. This factor was used for estimating the average 3D grain size from the mean 2D grain size.

3.2 Simulation Setup

The finite element analysis (FEA) was conducted with a commercial software (Ansys Workbench 19.2, Canonsburg, USA) to simulate the temperature distribution of the specimen inside the furnace during the experiment. Densification was not taken into account by this model. The geometry used in the simulation included all main features of the experimental setup of the loading dilatometry, in order to yield realistic results that reflect all heat transport processes inside the furnace (Figure 3). To save simulation

time, half of the 3D geometry was modelled and a corresponding symmetry condition was applied. The mesh was generated with quadrangular elements.

The thermal expansion coefficient was measured separately (+ 2K/min, 1400 °C, 30 min, - 2 K/min). The electrical resistivity of the specimen was measured during constant heating rate experiments. Figure 2 and Table 1 summarize the material properties used for this model. The boundary conditions of the model were the following: the top sample surface was set to different electrical potentials and the bottom sample surface was kept at 0 V. Heat losses through heat conduction between specimen and alumina disks (the temperature at the end of the alumina pushing rod was denoted in Figure 3) and heat radiation from sample surface, alumina disks and electrodes were taken into account. Samples were heated internally by Joule heating and externally by heating elements inside the furnace through the radiated heat transfer from the furnace to the sample.

Table 1: Material properties of 10YDC

Property	**10YDC**
Density [g/cm^3]	6.983
Thermal conductivity [W/mK]	12 [29]
Emmissivity	0.98

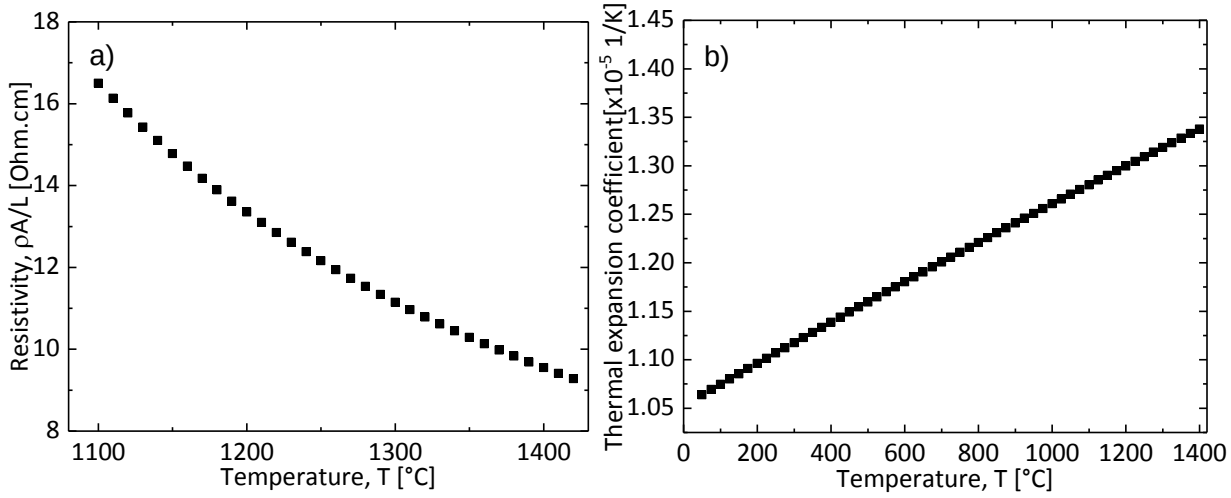

Figure 2: a) Resistivity of 10 YDC; b) coefficient of thermal expansion of 10YDC.

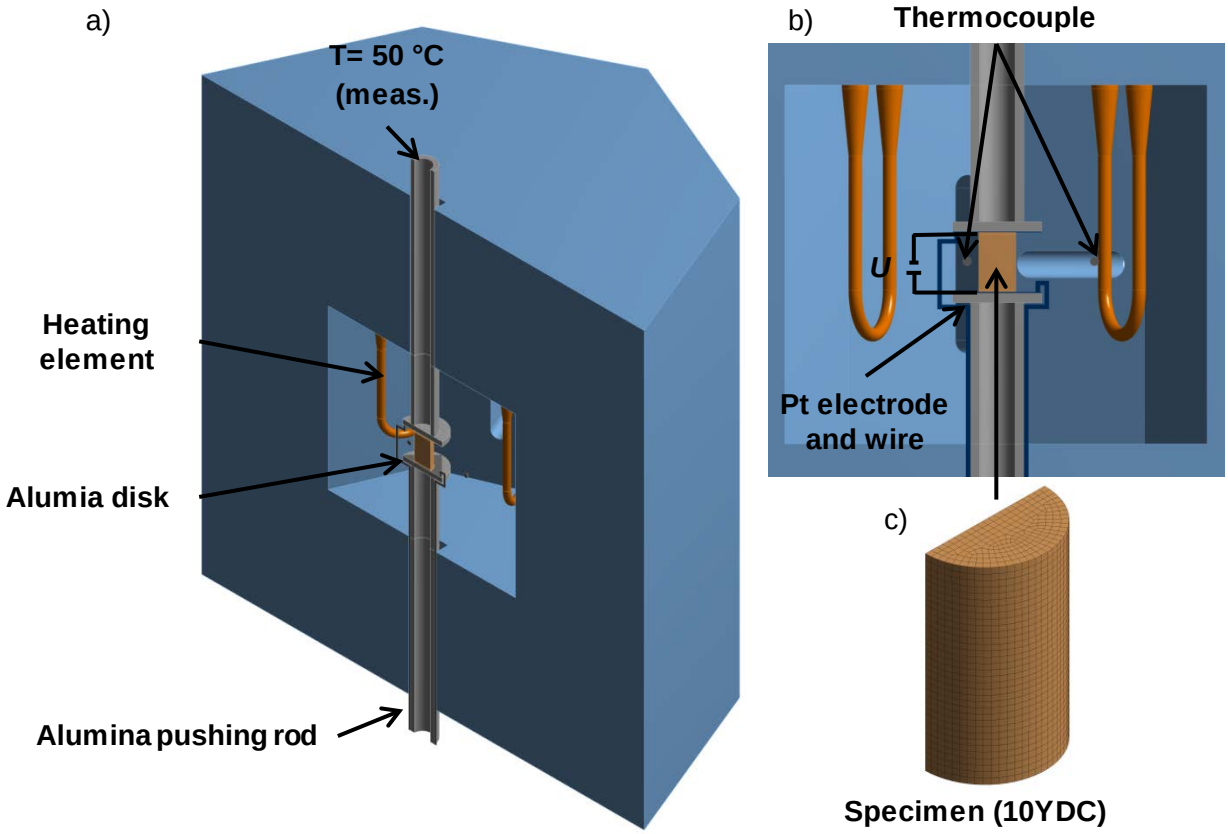

Figure 3: Finite element model of the loading dilatometry test frame a) isometric view; b) detailed front view of furnace chamber; c) mesh of the sample.

4 Results

4.1 Temperature Distribution

The corresponding temperature inside the sample (T2) as a function of the furnace temperature (T1) for different electrical field strengths is plotted in Figure 4a. As an illustration of the temperature inhomogeneity, the difference between the sample temperature (T2) and the temperature near the sample surface (T3) as a function of furnace temperature (T1) is shown as well (Figure 4b). The effect of Joule heating under E_{rms} = 14 V/cm was negligible. However, electric field strengths higher than 14V/cm introduced an obvious temperature increase inside the sample due to Joule heating effect. Smaller heat radiation at lower furnace temperature (1100 °C) led to the highest

temperature difference between T2 and T3, especially at higher electrical field strengths. This difference decreased when the furnace temperature increased. The comparison between the sample temperature (T2) and the simulation results is plotted in Figure 5. The given simulated temperature is the highest temperature at the symmetrical surface. The simulation results are in a good agreement with T2 of the experiments.

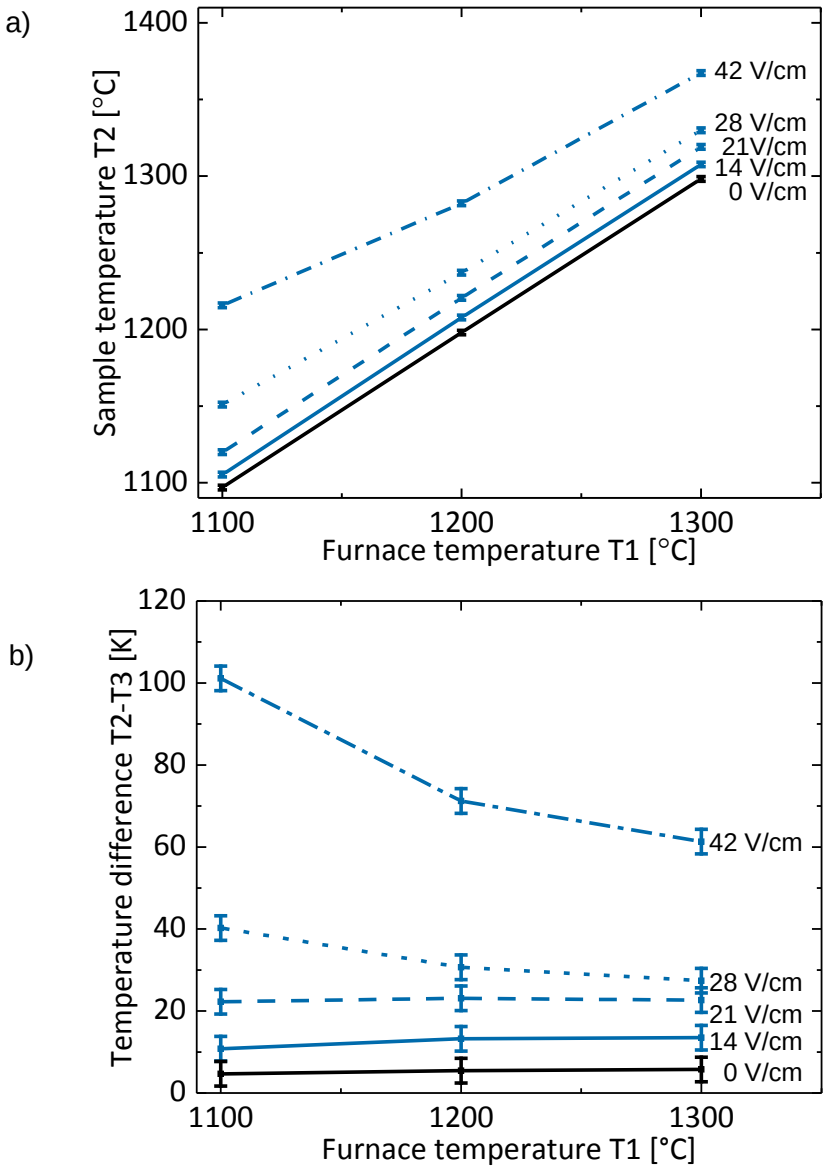

Figure 4: a) Inner sample temperature (T2) vs. furnace temperature (T1) under different electric fields. b) Difference between sample temperature (T2) and temperature near sample surface (T3) vs. furnace temperature (T1) under different electric fields.

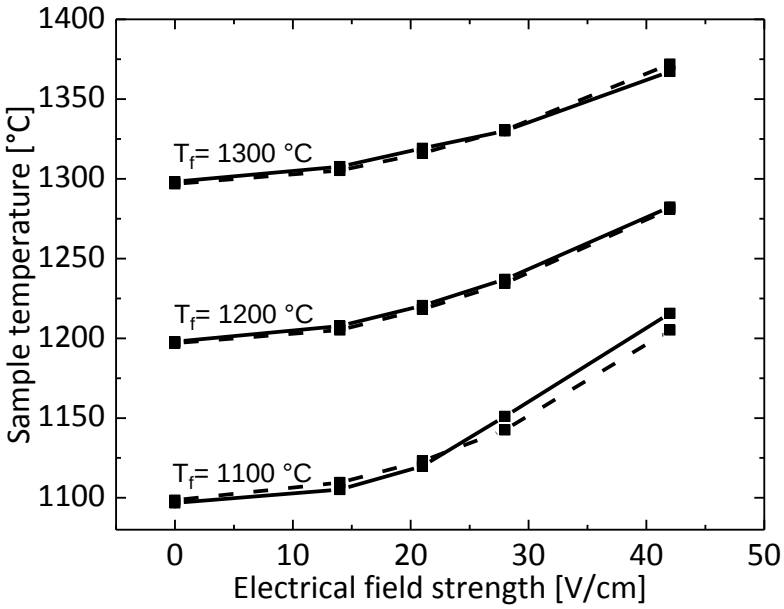

Figure 5: Comparison of sample temperature between simulation (dash lines) and experimental results (solid lines).

Isothermal furnace temperatures (T1) for the following sintering parameter measurements were determined on the base of T2 (Figure 6). A more complete overview of the temperature distribution of the sample was simulated for different electrical field strengths using the FEA. An example is shown in Figure 7 for E_{rms} = 28 V/cm. In order to maintain the same T2 under higher electrical field strengths, the temperature of the bottom and top of the sample as well as at the edge is lower than the temperature under 0 V/cm due to heat conduction between the sample and alumina disks and heat radiation, respectively. This leads to a lower average temperature (Table 2). Moreover, the comparison between simulation and experiments in power density and current density is given in Table 3.

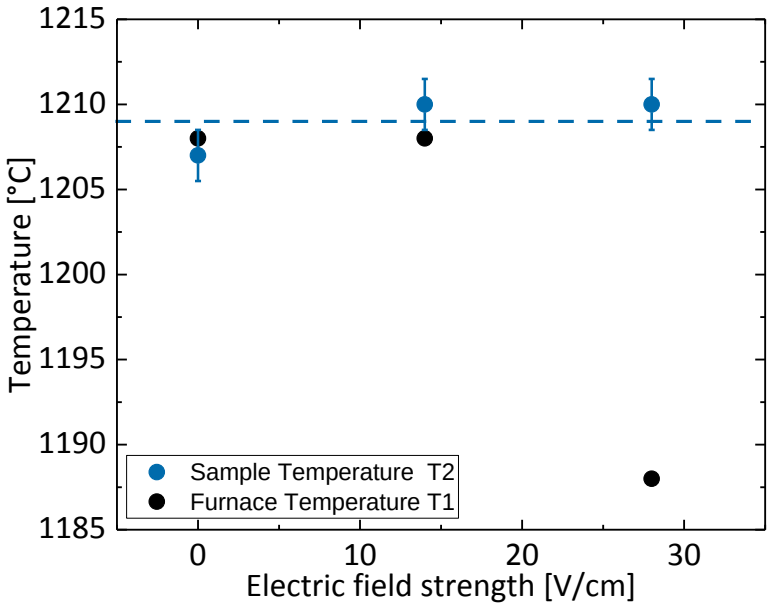

Figure 6: Experimental results of furnace temperatures (T1) to maintain the same sample temperature (T2) under different electric fields.

Table 2: Simulated results of the furnace temperature and the temperature distribution in the axisymmetric plane of the sample (including average, maximum and minimum temperature).

Electrical field strength V/cm	$T_{furnace}$	$T_{average}$	T_{max}	T_{max}-T_{min}
	°C			
0	1204	1204	1206	3
14	1203	1202	1205	11
28	1183	1189	1207	55

Table 3: Comparison of current density and power density between simulation and experiment.

Electrical field strength [V/cm]	**Current density [mA/mm^2]**		**Power density [mW/mm^3]**	
	simulation	experiment	simulation	experiment
14	11.7	11.2	16.2	16.8
28	20.0	21.1	55.4	60.0

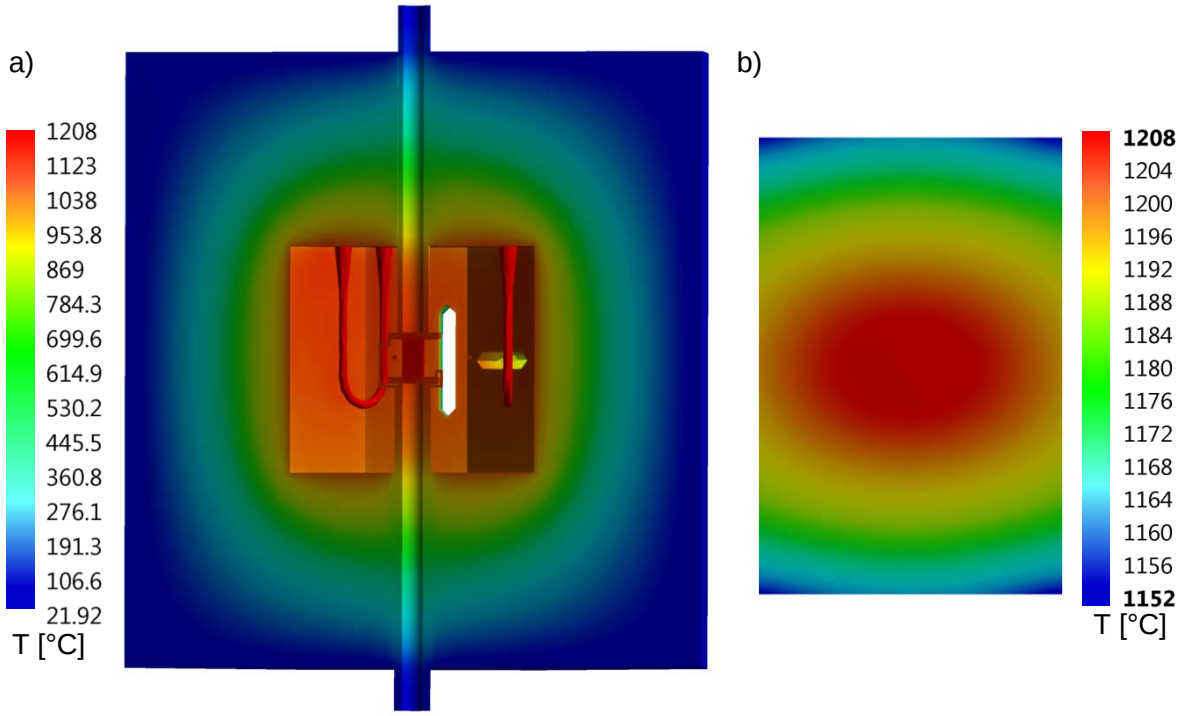

Figure 7: Simulation result of temperature distribution in loading dilatometry under E_{rms} = 28 V/cm with $T_{furnace}$ = 1188 °C: a) isometric view; b) detailed view of the sample.

4.2 Sintering parameter measurement

4.2.1 Shrinkage during sintering

The corresponding axial strain of free sintering vs. time as well as the calculated corresponding axial strain rate vs. density under different electrical field strengths are plotted in Figure 8 and Figure 9, respectively, which were necessary for the following calculations of sintering parameters. The electric field, applied voltage divided by the sample height vs. power density and current density as a function of sintering time are plotted in Figure 10.

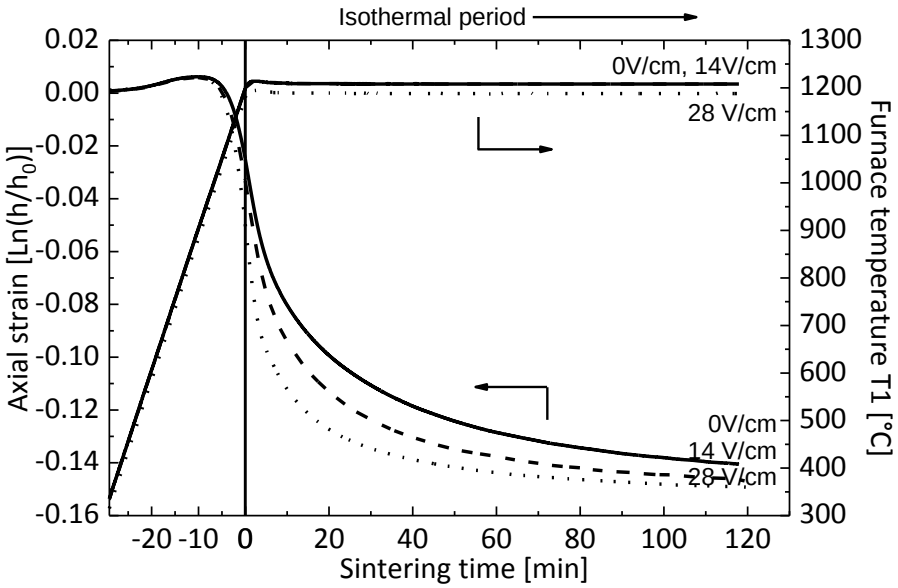

1

2 Figure 8: Axial strain and temperature as a function of time.

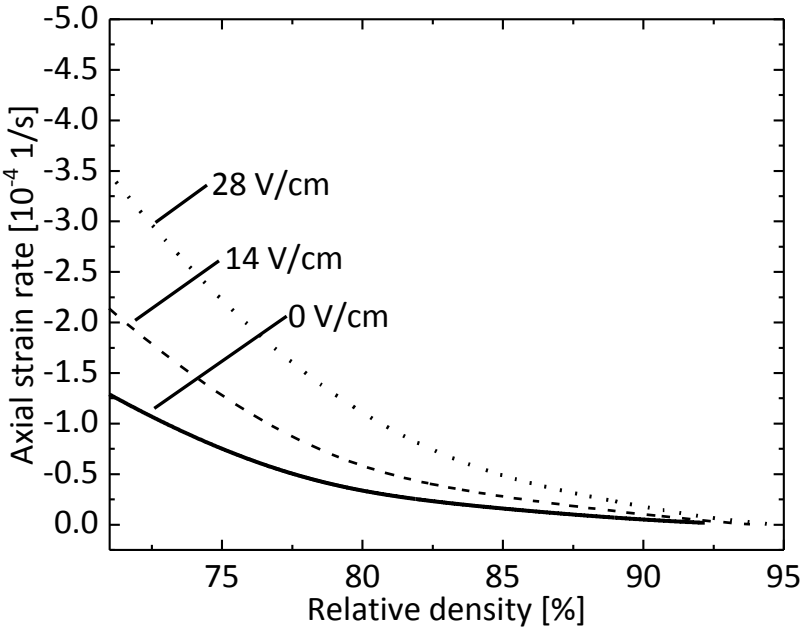

3

4 Figure 9: Axial strain rates with density under different electrical field strengths during
5 isothermal periods (under E_{rms} = 0 V/cm, 14 V/cm *and* 28 V/cm).

6

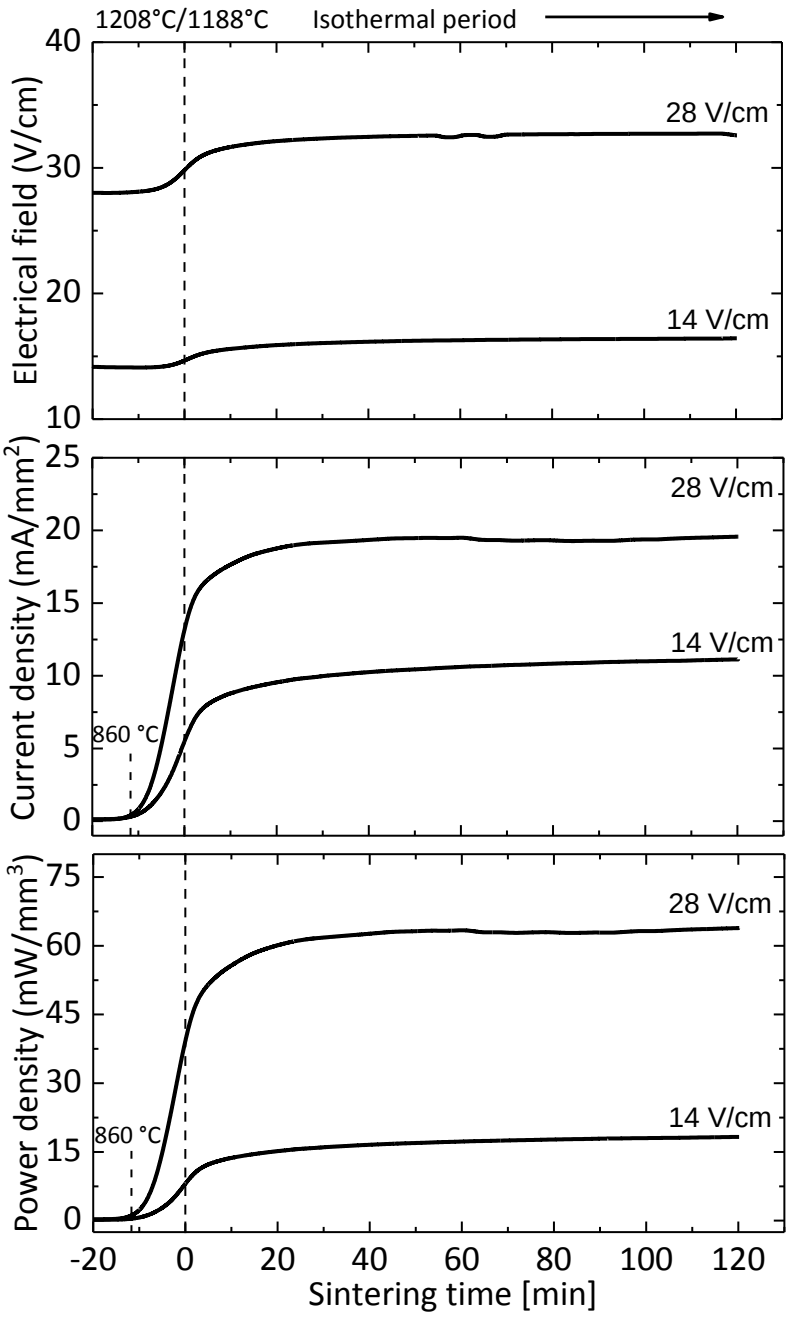

Figure 10: Electrical field, power density and current density over sintering time under E_{rms} = 14 V/cm and 28 V/cm.

The absolute value of power density and current density start to deviate from 0 at around 860 °C. The power density under E_{rms} = 28 V/cm increased by a factor of about 3.5 compared to the condition E_{rms} = 14 V/cm, whereas the current density increased by a factor of about 1.6. In contrast to the peak of power density appeared in flash sintering, the power density in our study increases until reaching a steady state during

the isothermal period. The highest power density under 28 V/cm is around 63 mW/mm^3 (Figure 10), significantly lower than the peak power density reported in flash sintering, which is typically 100-1000 mW/mm^3 [37]. Even though the electrical field increases due to the sample shrinkage, the current density is lower compared to the current density using dense specimens (Table 3), which is related to higher conductivity. The deviation from the densified sample in terms of power density is smaller than 12 % under these two electrical field strengths (Table 3). Therefore, even though the temperature was measured using densified samples, it can be assured that the macroscopic temperature of samples densifying under electrical fields is the same, or even lower than the case without electrical fields.

4.2.2 Calculation of uniaxial viscosity and uniaxial sintering stress

During the sintering parameter measurements, the linear relation between axial strain rate and uniaxial load was confirmed under electrical fields by applying three different loads at the relative density of 80 % under E_{rms} = 28 V/cm, as shown in Figure 11. The axial strain rate $\dot{\varepsilon}_z$ is presented as a function of the applied uniaxial stress for each density value. For each linear fit in Figure 11, the uniaxial viscosity and the sintering stress can be calculated according to Eq. 2.5-2.8. Uniaxial viscosity and sintering stress as a function of the relative density are plotted in Figure 12 and Figure 13, respectively. Taking the relative density of 80 % as an example, larger sintering stress and lower uniaxial viscosity were determined when an external electrical field was applied. Moreover, the influence of the electrical field on the sintering parameter is not directly proportional to the strength of applied electrical fields. At a fixed relative density (for example, 85 %), the uniaxial viscosity under E_{rms} = 14V/cm decreased by about a factor of 1.4, while E_{rms} = 28 V/cm prompted a decrease by about a factor of 2.4. The sintering stress under E_{rms} = 14 V/cm increased by a factor of about 1.18, while E_{rms} = 28V/cm induced a increase by a factor of about 1.26.

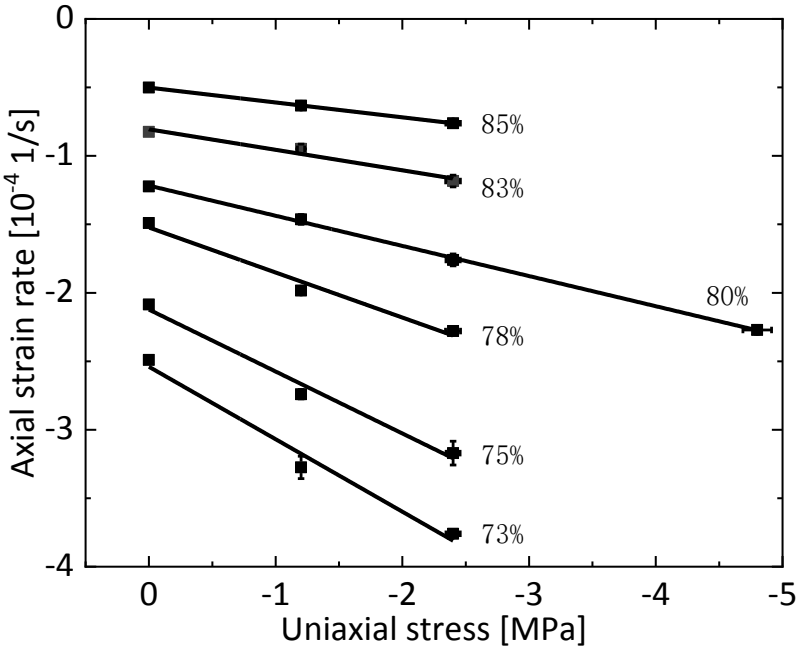

Figure 11: Axial strain rate as a function of uniaxial load for different relative densities at E_{rms} = 28 V/cm and $T_{furnace}$ = 1188 °C. A fourth load was applied at the relative density of 80 % to prove the linear dependency.

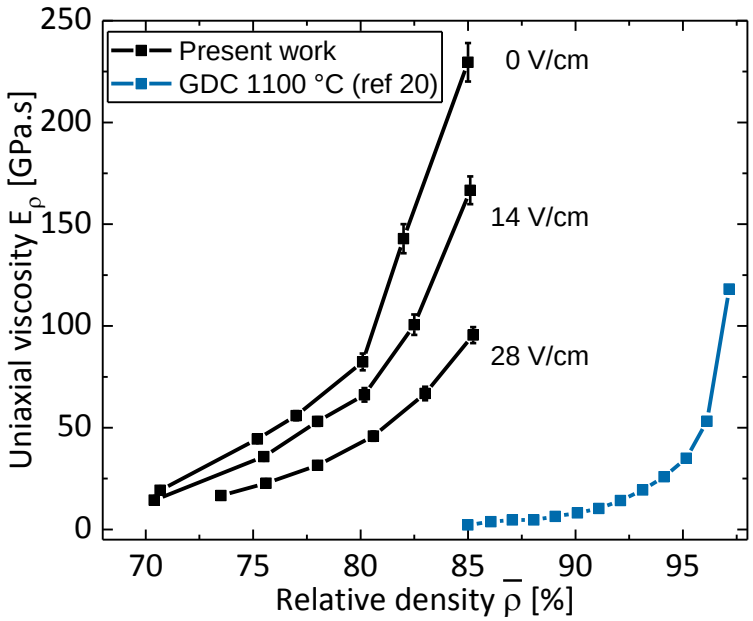

Figure 12: Uniaxial viscosity as a function of relative density using discontinuous sinter-forging. Comparison of the measured uniaxial viscosity as a function of relative density

under different electrical fields in our work with the uniaxial viscosity of nanocrystalline gadolinium-doped ceria [25].

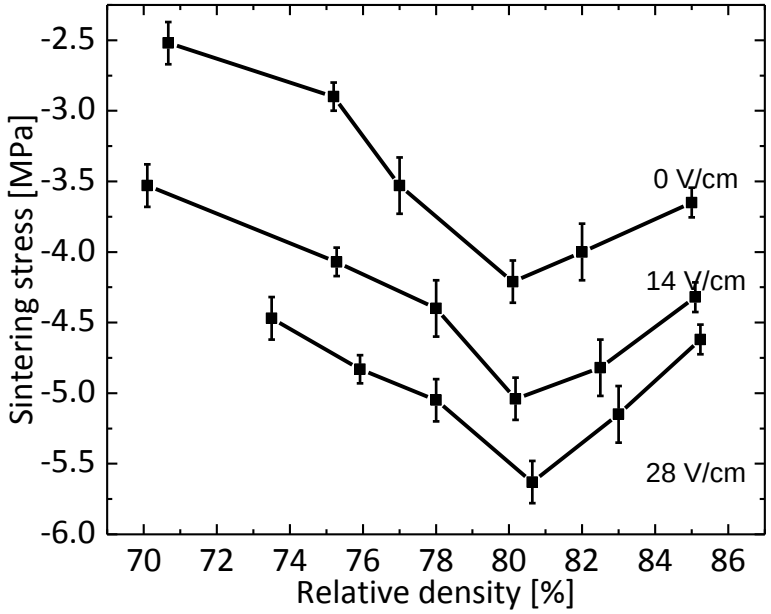

Figure 13: Sintering stress as a function of relative density using discontinuous sinter-forging.

4.2.3 Microstructure analysis

Grain size of samples after discontinuous sinter-forging experiments under 2.4MPa is depicted in Figure 14. No obvious grain growth is observed up to a relative density of 84%. The grain sizes during sintering under different electrical field strengths do not significantly differ in this range considering the margin of error of the grain size analysis.

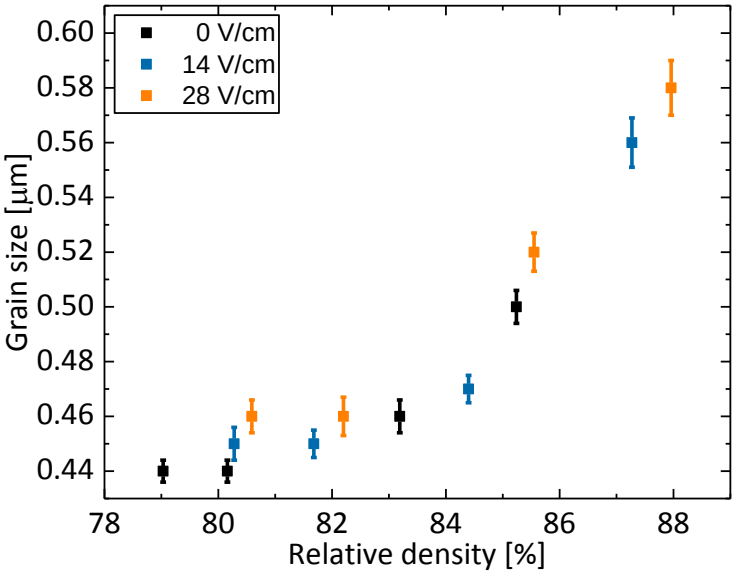

Figure 14: Sintering trajectory of grain size of samples after discontinuous sintering forging experiments with E_{rms} = 0 V/cm, 14 V/cm and 28 V/cm as a function of relative density.

5 Discussion

The results in this study have shown a field related improvement in shrinkage and sintering rate for a given density and at a constant sample temperature, even under electrical fields lower than the 'flash regime' (Figure 8 and Figure 9). The application of electrical field also resulted in a decrease in the uniaxial viscosity and an increase in the uniaxial sintering stress, even without any macroscopic Joule heating effect. This was achieved by keeping the highest temperature inside the densified sample constant under different electrical field strengths and confirmed by the simulated temperature distribution profile (Table 2). According to thermal-electric finite element simulation, the average temperature (with the same T2) inside the sample is even lower under higher electric fields (Table 2). It is important to note that both temperature measurements and simulation were conducted on the base of densified specimen with a higher conductivity and corresponding higher current and power density. It is therefore equivalent that the highest temperature inside a densifying sample is even lower, because the power and current density increases with densification and reaches its maximal value at the

highest relative density. However, under the precondition that the same highest temperature of densified sample with and without electrical fields is constant, it is plausible to assume same temperature or even lower temperature under electrical fields.

According to Figure 12, the measured uniaxial viscosity first increases slowly with respect to relative density until it reaches 80%. Then, it increases progressively for further relative density increase. This behavior is observed for all conditions, i.e. with and without electrical fields. According to Eq 2-6, the dependency of the second term, $E_{p1}(\rho)$, on relative density expresses the low uniaxial viscosity at relative densities lower than 90 % [27,38-41]. The effects of grain coarsening on uniaxial viscosity are expressed by the third term, $E_{p2}(d)$. It is proportional to the cube of the grain size for the case of grain boundary diffusion [23]. The measured viscosity of nanocrystalline gadolinium-doped ceria sample at 1100 °C with an initial grain size of 35 nm also showed the same trend [25] (Figure 12). However, our measured results differ from the above mentioned work in the range of relative density. The difference can be attributed to a more homogenous powder compacts and smaller initial grain size, which not only lead to a lower uniaxial viscosity but also to a smaller grain size (around 300 nm at a relative density of 98 %). In addition, the different dopant element Y instead of Gd may also modify the sintering behavior.

Rahaman [41] proposed a model for uniaxial viscosity based on experiments conducted by loading dilatometry. According to the moderate sintering temperatures and fine grain size of the powder investigated here, we assume that grain boundary diffusion is the main sintering mechanism, as found by sinter-forging experiments for nanocrystalline gadolinium-doped ceria [25]. Therefore, this model was derived by combining Coble's creep mechanism [41-42], i.e. grain boundary diffusion and Beere's [43-44] calculation of the stress intensification factor, Φ, considering a more complicated geometry of pores in the microstructure. To compare the measured viscosity with this model, the sintering trajectory has to be considered (Figure 14), showing grain growth after a relative density of 84 %. At lower densities, the grain size remains 0.45 µm. The calculation of uniaxial viscosity is provided as follows [41]:

$$E_p = E_{p0} \times E_{p1}(\rho) \times E_{p2}(d) = A \times \bar{\rho} \frac{exp[-3a(1-\bar{\rho})]}{3\,exp[-a(1-\bar{\rho})]+exp[-2a(1-\bar{\rho})]} \times d^3 \quad (5\text{-}1)$$

where A is a scaling factor, d is the grain size, $\bar{\rho}$ is the relative density and a is a parameter related to the dihedral angle. Additionally, the viscosity dependence on temperature is decided by a fourth term, $E_{p3}(T)$ [45]:

$$E_p = E_{p0} \times E_{p1}(\rho) \times E_{p2}(d) \times E_{p3}(T), \text{ with } E_{p3}(T) = \exp\left(\frac{Q_{E_p}}{RT}\right) \quad (5\text{-}2)$$

The model was at first used to fit the uniaxial viscosity without electrical field. The parameter, a, was fitted to be 6.8 in this study. Chang used 10.5 for GDC [25], Rahaman reported 5 for ZnO and 2 for CdO [41]. In Beere's model, a is inversely proportional to the dihedral angle. Following this principle, the dihedral angle in this work should be larger than 116 ± 4 ° as reported by Chang for GDC [25]. Then, the uniaxial viscosities under the other two electrical field strengths were calculated using the same parameters, A and a, and the measured grain sizes. Subsequently, under the assumption that the activation energy (420 kJ/mol reported by Kinamuchi [46] for submicron ceria) is not changed under electric fields, the fourth term, E_{p3} was considered and the fictive sample temperature was adjusted until obtaining a good fitting between model and experiments (as shown in Figure 15). The fictive temperature was 22 K and 47 K higher for 14 V/cm and 28 V/cm, respectively, than the specimen temperature without applied field. This enables to quantify and validate the effect of applied electric fields in terms of equivalent thermal energy transferred to the sample, but does not give any hint about the real nature of the electrical field effect.

The model shows a good agreement with the measured data (the difference remains less than 15 % up to a relative density of 84 %), except for the highest relative density of 85 % under electrical fields, where the uniaxial viscosity was overestimated. Possible explanations for the effect of electric field or sintering parameters are: change in the grain boundary structure and the activation energy for grain boundary diffusion, temperature microgradients (as macroscopic Joule heating is excluded).

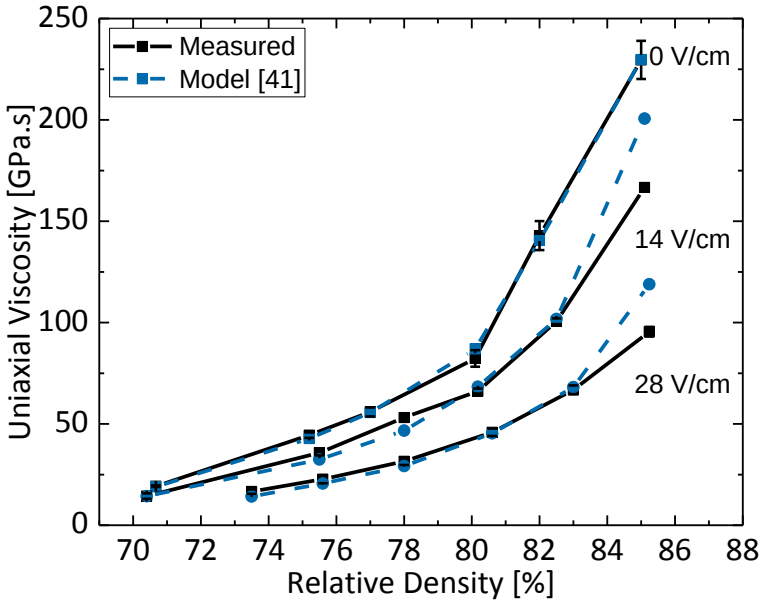

Figure 15: Comparison between measured uniaxial viscosity and theoretical prediction, introducing a fictive temperature increase in the presence of electric fields.

According to Figure 13, the absolute value of measured sintering stress first increases and then decreases, the transition range lying between relative density of 80 % and 84 %. It corresponds approximately to the onset of pronounced grain growth, which is consistent to the grain size analysis. Considering an idealized microstructure, the basic form for sintering potential can be expressed as follows [23,31]:

$$\Sigma = \frac{2\Upsilon_{GB}}{d} + \frac{2\Upsilon_S}{r} \tag{5-3}$$

where Υ_s and Υ_{GB} are surface energy and grain boundary energy, respectively, and d and r are grain size and radius of the curvature of pores. At low relative densities, smaller pores with larger surface curvatures dominate the microstructure and the sintering stress increases along with the decreasing surface curvature. At higher relative densities, the decrease of the number of pores and especially the coarsening of the grains explains the decrease of sintering stress. As shown here for grain size and in another piece of work [47], microstructure including pore orientation is not modified by applied stress and electric fields. This means that electric field could modify both grain boundary and surface energies, resulting in the measured increased sintering stress.

Ghosh et al. [48] suggested that grain boundary interfacial energy can be expressed as:

$$\Upsilon_{GB} = \Delta H_{GB} - T\Delta S_{GB} \quad (5\text{-}5)$$

where ΔH_{GB} and ΔS_{GB} are the excess of enthalpy and entropy, respectively, associated with the grain boundary. According to this equation, a higher local temperature would lead to a lower grain boundary energy, due to the positive excess entropy of the boundary. This was experimentally verified by a slight decrease of relative grain-boundary energy (Υ_{GB}/Υ_s) of alumina from 1450 °C to 1650 °C of about 6 % [49]. Tsoga and Pnikolopoulos used the multiphase equilibration technique to determine the surface energy as well as the grain boundary energy of the equilibrium angles of polycrystalline yttria-stabilized zirconia from 1300 °C to 1600 °C, and also concluded that both surface energy and grain boundary energy decreased linearly according to the temperature [50]. However, it is unconceivable to conclude that higher electrical fields lead to lower local temperatures. According to the above discussion, a localized temperature gradient cannot be the only explanation for the measured results. Moreover, the numerical simulation of mixed or ionically conducting ceramics shows no significant contribution of high temperature gradient induced by high current flow of 10^4 A/m^2 [51], as they are limited to a few degrees (smaller than 10 K). Even though in the work of Schwesig [8], density fluctuation in the microstructure of nanocrystalline silicon was used as an indication of existence of the microscopic temperature gradient, no quantification of the temperature increase was given.

6 Conclusions

1. The discontinuous sinter-forging technique was applied for the first time to measure sintering parameters under electric fields. The combination of measurement by thermocouple of the sample temperature and thermo-electric finite element simulations ensured that the macroscopic Joule heating effect was excluded.
2. Moderate electrical fields improve the sintering behavior, decrease uniaxial viscosity and increase the sintering stress.
3. The significantly enhanced sintering behavior observed under fields well below the flash regime can have several origins: gradual modification of the grain

boundary structure (including space charge layer) and properties or a local temperature gradients which are not detected at macroscopic scale.

Acknowledgement

The authors acknowledge funding from the German Science Foundation (DFG), under priority program “Fields Matter” SPP 1959 [GU 933/9-1].

7 Reference

[1]. O. Guillon, C. Elsässer, O. Gutfleisch, J. Janek, S. Korte-Kerzel, D. Raabe, C.A. Volkert, Manipulation of matter by electric and magnetic fields: Toward novel synthesis and processing routes of inorganic materials, Mater. Today. 21(2018) 527-536.

[2]. O. Guillon, J. Gonzalez-Julian, B. Dargatz, T. Kessel, G. Schierning, J. Räthel, M. Herrmann, Field-Assisted Sintering Technology/Spark Plasma Sintering: Mechanisms, Materials, and Technology Developments, Adv. Eng. Mater. 16(2014) 830-849.

[3]. M. Biesuz, V.M. Sglavo, Flash sintering of ceramics, J. Eur. Ceram. Soc. 39(2019) 115-143.

[4]. J. Langer, M.J. Hoffmann, O. Guillon, Direct comparison between hot pressing and electric field-assisted sintering of submicron alumina, Acta Mater. 57(2009) 5454-5465.

[5]. J. Langer, M.J. Hoffmann, O. Guillon, Electric Field-Assisted Sintering in Comparison with the Hot Pressing of Yttria-Stabilized Zirconia, J. Am. Ceram. Soc. 94(2011) 24-31.

[6]. T.B. Holland, T.B. Tran, D.V. Quach, U. Anselmi-Tamburini, J.R. Groza, A.K. Mukherjee, Athermal and thermal mechanisms of sintering at high heating rates in the presence and absence of an externally applied field, J. Eur. Ceram. Soc. 32(2012) 3675-3683.

[7]. B. McWilliams, A. Zavaliangos, Multi-phenomena simulation of electric field assisted sintering, Journal of Materials Science. 43(2008) 5031-5035.

[8]. D. Schwesig, G. Schierning, R. Theissmann, N. Stein, N. Petermann, H. Wiggers, R. Schmechel, D.E. Wolf, From nanoparticles to nanocrystalline bulk: percolation effects in field assisted sintering of silicon nanoparticles, Nanotechnology. 22(2011) 135601.

[9]. R. Kirchheim, On the mixed ionic and electronic conductivity in polarized yttria stabilized zirconia, Solid State Ionics. 320(2018) 239-258.

[10]. J. Chun, M. Martin, H.-I. Yoo, On the kinetic decomposition voltage of ternary oxides, PCCP. 20(2018) 2396-2402.

[11]. M. Cologna, B. Rashkova, R. Raj, Flash Sintering of Nanograin Zirconia in <5 s at 850°C, J. Am. Ceram. Soc. 93(2010) 3556-3559.

[12]. J.G. Pereira da Silva, J.M. Lebrun, H.A. Al‐Qureshi, R. Janssen, R. Raj, Temperature Distributions During Flash Sintering of 8% Yttria‐Stabilized Zirconia, J. Am. Ceram. Soc. 98(2015) 3525-3528.

[13]. M. Schie, S. Menzel, J. Robertson, R. Waser, R.A. De Souza, Field-enhanced route to generating anti-Frenkel pairs in HfO_2, Phys. Rev. Mater. 2(2018) 035002.

[14]. Y. Zhang, J.-I. Jung, J. Luo, Thermal runaway, flash sintering and asymmetrical microstructural development of ZnO and ZnO–Bi_2O_3 under direct currents, Acta Mater. 94(2015) 87-100.

[15]. R.I. Todd, E. Zapata-Solvas, R.S. Bonilla, T. Sneddon, P.R. Wilshaw, Electrical characteristics of flash sintering: thermal runaway of Joule heating, J. Eur. Ceram. Soc. 35(2015) 1865-1877.

[16]. Y. Dong, I.W. Chen, Onset Criterion for Flash Sintering, J. Am. Ceram. Soc. 98(2015) 3624-3627.

[17]. J.G.P. da Silva, H.A. Al-Qureshi, F. Keil, R. Janssen, A dynamic bifurcation criterion for thermal runaway during the flash sintering of ceramics, J. Eur. Ceram. Soc. 36(2016) 1261-1267.

[18]. M. Tokita, Recent and future progress on advanced ceramics sintering by Spark Plasma Sintering, Nanotechnologies in Russia. 10(2015) 261-267.

[19]. W. Ji, B. Parker, S. Falco, J.Y. Zhang, Z.Y. Fu, R.I. Todd, Ultra-fast firing: Effect of heating rate on sintering of 3YSZ, with and without an electric field, J. Eur. Ceram. Soc. 37(2017) 2547-2551.

[20]. J.C. M'Peko, J.S.C. Francis, R. Raj, Impedance Spectroscopy and Dielectric Properties of Flash Versus Conventionally Sintered Yttria-Doped Zirconia Electroceramics Viewed at the Microstructural Level, J. Am. Ceram. Soc. 96(2013) 3760-3767.

[21]. Y. Du, A.J. Stevenson, D. Vernat, M. Diaz, D. Marinha, Estimating Joule heating and ionic conductivity during flash sintering of 8YSZ, J. Eur. Ceram. Soc. 36(2016) 749-759.

[22]. C. Schmerbauch, J. Gonzalez-Julian, R. Röder, C. Ronning, O. Guillon, Flash Sintering of Nanocrystalline Zinc Oxide and its Influence on Microstructure and Defect Formation, J. Am. Ceram. Soc. 97(2014) 1728-1735.

[23]. R. Zuo, E. Aulbach, J. Rödel, Experimental determination of sintering stresses and sintering viscosities, Acta Mater. 51(2003) 4563-4574.

[24]. J.-B. Ollagnier, O. Guillon, J. Rödel, Viscosity of LTCC Determined by Discontinuous Sinter-Forging, International Journal of Applied Ceramic Technology. 3(2006) 437-441.

[25]. J. Chang, O. Guillon, J. Rödel, S.-J.L. Kang, Uniaxial viscosity of gadolinium-doped ceria determined by discontinuous sinter forging, J. Eur. Ceram. Soc. 27(2007) 3127-3133.

[26]. R.K. Bordia, G.W. Scherer, On constrained sintering—II. Comparison of constitutive models, Acta Metall. 36(1988) 2399-2409.

[27]. R. Zuo, E. Aulbach, R.K. Bordia, J. Rödel, Critical Evaluation of Hot Forging Experiments: Case Study in Alumina, J. Am. Ceram. Soc. 86(2003) 1099-1105.

[28]. R. Raj, R.K. Bordia, Sintering behavior of bi-modal powder compacts, Acta Metall. 32(1984) 1003-1019.

[29]. R.K. Bordia, G.W. Scherer, On constrained sintering—I. Constitutive model for a sintering body, Acta Metall. 36(1988) 2393-2397.

[30]. Z.Z. Du, A.C.F. Cocks, Constitutive models for the sintering of ceramic components—I. Material models, Acta Metallurgica et Materialia. 40(1992) 1969-1979.

[31]. R. Raj, Analysis of the Sintering Pressure, J. Am. Ceram. Soc. 70(1987) C-210-C-211.

[32]. L.C. De Jonghe, M.N. Rahaman, Sintering of Ceramics, in: F. Aldinger, N. Claussen, R.M. Spriggs, K. Uchino, K. Koumoto, and M. Kaneno, (Eds), Handbook of Advanced Ceramics, Academic Press, Oxford, 2003, pp. 187-264.

[33]. G. Okuma, J. Gonzalez-Julian, O. Guillon, F. Wakai, Comparison between sinter forging and X-ray microtomography methods for determining sintering stress and bulk viscosity, J. Eur. Ceram. Soc. 38(2018) 2053-2058.

[34]. R. Zuo, E. Aulbach, J. Rödel, Continuum Mechanical Approach to Sintering of Nanocrystalline Zirconia, Adv. Eng. Mater. 7(2005) 949-952.
[35]. J. Kanters, U. Eisele, J. Rödel, Cosintering Simulation and Experimentation: Case Study of Nanocrystalline Zirconia, J. Am. Ceram. Soc. 84(2001) 2757-2763.
[36]. A.R.C. Gerlt, A.K. Criner, L. Semiatin, E.J. Payton, On the grain size proportionality constants calculated in M.I. Mendelson's “Average Grain Size in Polycrystalline Ceramics”, J. Am. Ceram. Soc.
[37]. M. Yu, S. Grasso, R. McKinnon, T. Saunders, M.J. Reece, Review of flash sintering: materials, mechanisms and modelling, Advances in Applied Ceramics. 116(2017) 24-60.
[38]. J. Svoboda, H. Riedel, H. Zipse, Equilibrium pore surfaces, sintering stresses and constitutive equations for the intermediate and late stages of sintering—I. computation of equilibrium surfaces, Acta Metallurgica et Materialia. 42(1994) 435-443.
[39]. H. Riedel, H. Zipse, J. Svoboda, Equilibrium pore surfaces, sintering stresses and constitutive equations for the intermediate and late stages of sintering—II. Diffusional densification and creep, Acta Metallurgica et Materialia. 42(1994) 445-452.
[40]. K.R. Venkatachari, R. Raj, Shear Deformation and Densification of Powder Compacts, J. Am. Ceram. Soc. 69(1986) 499-506.
[41]. M.N. Rahaman, L.C. De Jonghe, R.J. Brook, Effect of Shear Stress on Sintering, J. Am. Ceram. Soc. 69(1986) 53-58.
[42]. R.L. Coble, W.D. Kingery, Effect of Porosity on Physical Properties of Sintered Alumina, J. Am. Ceram. Soc. 39(1956) 377-385.
[43]. W. Beere, A unifying theory of the stability of penetrating liquid phases and sintering pores, Acta Metall. 23(1975) 131-138.
[44]. W. Beere, The second stage sintering kinetics of powder compacts, Acta Metall. 23(1975) 139-145.
[45]. R. Zuo, J. Rödel, Temperature dependence of constitutive behaviour for solid-state sintering of alumina, Acta Mater. 52(2004) 3059-3067.

[46]. Y. Kinemuchi, K. Watari, Dilatometer analysis of sintering behavior of nano-CeO_2 particles, J. Eur. Ceram. Soc. 28(2008) 2019-2024.

[47]. C. Cao, R. Mücke, O. Guillon, Evolution of viscous Poisson's ratio, bulk and shear viscosities during electric field assisted sintering of polycrystalline ceria, (under preparation).

[48]. S. Ghosh, A.H. Chokshi, P. Lee, R. Raj, A Huge Effect of Weak dc Electrical Fields on Grain Growth in Zirconia, J. Am. Ceram. Soc. 92(2009) 1856-1859.

[49]. M.N. Kelly, S.A. Bojarski, G.S. Rohrer, The temperature dependence of the relative grain-boundary energy of yttria-doped alumina, J. Am. Ceram. Soc. 100(2017) 783-791.

[50]. A. Tsoga, P. Nikolopoulos, Surface and grain-boundary energies in yttria-stabilized zirconia (YSZ-8 mol%), Journal of Materials Science. 31(1996) 5409-5413.